Hindawi
Structural Control and Health Monitoring
Volume 2024, Article ID 7255774, 20 pages
https://doi.org/10.1155/2024/7255774

Research Article

Pole-Placement-Based Calibration of an Electromagnetically Realizable Inerter-Based Vibration Absorber (IDVA) for Rotating Wind Turbine Blades

Zili Zhang,[1,2] **Xiang Li**,[1] **Tobias Greve Larsen**,[3] **Tao Sun**,[4] **and Qingshan Yang**[5]

[1]*College of Civil Engineering, Tongji University, Shanghai 200092, China*
[2]*State Key Laboratory of Disaster Reduction in Civil Engineering, Shanghai 200092, China*
[3]*Wood Thilsted Partners Limited, Aarhus 8000, Denmark*
[4]*College of Engineering, Ocean University of China, Qingdao 266100, China*
[5]*School of Civil Engineering, Chongqing University, Chongqing 400045, China*

Correspondence should be addressed to Tao Sun; suntao@ouc.edu.cn

Received 17 September 2023; Revised 13 November 2023; Accepted 13 January 2024; Published 3 February 2024

Academic Editor: Francesc Pozo

This paper deals with edgewise vibration mitigation of rotating wind turbine blades by means of inerter-based vibration absorber (IDVA), which can be realized both mechanically and electromagnetically. Introducing the electromagnetically-realizable IDVA to the blade forms a 3-degree-of-freedom (3-DOF) blade-IDVA system consisting of the rotating blade, an absorber, and a series inerter-dashpot-spring subsystem. Analytical optimal design formulas of the rotating blade-installed IDVA are then derived using a pole-placement method where the equal-modal-damping-ratio principle and the triple-root-bifurcation condition are applied. The analytical formulas show that the optimal parameters for the blade-IDVA system merely depend on the spinning speed of the rotor given the IDVA location and the absorber mass. Numerical results of the NREL 5 MW wind turbine with optimal IDVA show that optimal IDVA leads to superior performance than optimal TMD in mitigating the blade edgewise vibration and behaves nearly as same as optimal RIDTMD, along with slightly optimal damper parameters variation. This means that the inerter-dashpot-spring system can be deployed flexibly for damping edgewise vibrations of rotating blades.

1. Introduction

Modern megawatts wind turbines are designed to be larger and installed at deep-sea sites to capture more wind energy, leading to higher capacity and lower cost. Large-scale wind turbines with taller towers and flexible blades make the structural dynamic response more susceptive to external wind and wave loadings, which may reduce the fatigue life and power production for wind turbine system [1], especially for the lightly damped edgewise vibration of wind turbine blades. The main blade vibration modes are flapwise and edgewise. Different control methods and damper devices were studied for reducing blade flapwise vibrations [2–5]. In fact, the blade flapwise vibration is mainly quasi-static due to the high flapwise modal damping caused by the aerodynamic damping. Out of the two, edgewise vibrations can be of significant concern in wind turbines. Generally, the damping in edgewise mode consists of the structural damping and the aerodynamic damping, while the latter can be negligible [6, 7] due to the aerodynamic shape of the blade [8]. Therefore, the total damping in edgewise mode will be low and even become negative, which leads to the aerodynamic instability [9–11] and even structural damages or failures [12]. In the past five years, there has been an extremely rapid development in the increase of blade lengths, with reducing the levelized cost of energy (LCOE) as almost the only goal. As a consequence, currently, the wind industry is unfortunately facing severe challenges regarding the blade edgewise vibrations of wind turbines with the rate ranging from 5 MW to 8 MW, both onshore and offshore.

To mitigate the vibration of wind turbine blades in the edgewise direction, the extra damping is required, which can be achieved through aerodynamic control devices or structural control devices. Aerodynamic control devices such as the stall strips [13], the microtabs [14], and the vortex generators [15] are used to tune lift coefficients of the airfoil by modifying the blade geometric shape. Hence, they predominantly tune the flapwise blade loads, while hardly affecting the lightly damped edgewise vibration, and may have a negative influence on the power output [13]. To the end, different structural control devices are designed to effectively increase the damping in the edgewise mode such as the roller damper [16], the tuned liquid damper (TLD) [17, 18], the circular liquid column damper (CLCD) [19], the tuned liquid column damper (TLCD) [20, 21], magnetorheological (MR) dampers [22], and shunt dampers [23, 24]. Their performance of edgewise vibration mitigation had been demonstrated numerically or experimentally. Furthermore, different control technologies are applied to structural control devices to improve the vibration mitigation performance, including active, semiactive, and passive methods. This method has attracted much attention because of its efficient vibration mitigation performance, which can be achieved through simple and cost-efficient configurations. Different types of active, semiactive, and passive dampers were designed to mitigate the edgewise vibration of rotating blades. Staino et al. [25] designed active tendons to reduce the blade edgewise vibrations. A linear control law was used to determine the active tendon forces to respond to the variation of aerodynamic loads. Fitzgerald et al. [26] analyzed the superior performance of active tuned mass dampers (ATMDs) with LQR-based control strategy to mitigate the edgewise vibration. Krenk et al. [27] proposed an active strut to suppress the wind-induced blade edgewise vibrations. An active controller for coupling the rotor was developed using the resonance principle. Van-Nguyen et al. [28] proposed semiactive tuned mass dampers (STMDs) to control the blade edgewise vibrations for spar-type floating wind turbines. A semiactive control strategy was performed where the optimized STMD stiffness was obtained via the short-time Fourier transform (STFT) algorithm. Chen et al. [22] introduced MR dampers to dissipate energy inside the wind turbine blade to reduce the edgewise vibration under extreme wind loads where semiactive fuzzy control is used to produce the desired force. Biglari and Fakhari [23] proposed a passive shunt damper to reduce the edgewise vibration of the wind turbine blades, and a genetic algorithm was used for damper design. The result demonstrated the improved effectiveness of the proposed damper compared with the conventional TMD. Park and Lackner [29] investigated the vibration mitigation for multimegawatt wind turbine blades in the edgewise direction under passive TMDs, demonstrating their potential benefits and impacts. In these studies, different damper devices are introduced to wind turbine blades, forming a coupling blade-damper system, and numerical optimizations are applied to the coupling system for damper design. In practice, the use of numerical optimization for damper design of the blade-damper system leads to issues related to the computational burden. More importantly, the optimal damper parameters change with the varying rotor operational conditions, making it impossible for the numerical optimization technique to cover all operational conditions (in theory, infinite numbers of conditions).

To circumvent these issues, closed-form optimal turning formulas were derived for some blade-installed dampers, facilitating optimal design of the damper for any rotor speed. Zhang [30] derived the explicit optimal tuning formulas for the TMD to reduce the blade edgewise vibration. To derive the optimal frequency-tuning formulas, two different optimality criteria are introduced, the equal modal damping ratio and the equal dynamic amplification, while the optimal TMD damping ratio was derived via dynamic amplification analysis and was proven to be related to the rotor rotational speed. Subsequently, Zhang and Fitzgeral [31] introduced the tuned mass-damper-inerter (TMDI) for improving the blade edgewise vibration mitigation for wind turbine by means of the mass-amplification effect of the inerter. Two ends of the inerter were connected to the TMD and the blade structure separately. The explicit formulas for the optimal damping ratio and frequency ratio were determined through frequency response analysis. More recently, Zhang and Larsen [32] utilized the characteristics of the inerter to come up with a new type of damper, the RIDTMD (rotational inertia double tuned mass damper), for blade in-plane vibration mitigation where a tuned viscous mass damper is used in place of the viscous damper in a classical TMD (the inerter is in parallel with a dashpot while in series with a spring). They established the explicit formulas for the RIDTMD optimal calibration and demonstrated its superior performance in mitigating blade edgewise vibrations compared with the optimal TMD. It is worth noting that all these inerter-based devices are realized mechanically and may face practical challenges when being installed inside the hollow blade with space constraints. Furthermore, the potential of semiactive control has not been explored. Therefore, an alternative inerter-based device that can be realized electromagnetically is of great interest, as it can potentially address these two points.

In the present paper, an inerter-based vibration absorber (IDVA) that can be realized both mechanically and electromagnetically is proposed for edgewise vibration mitigation of a rotating blade. Closed-form optimal design formulas are derived for the rotating wind turbine blade-equipped IDVA, where the IDVA device consists of an absorber elastically bonded to the blade structure and a series inerter-dashpot-spring system. The 3-degree-of-freedom (3-DOF) blade-IDVA system consisting of the rotating blade, an absorber, and a series inerter-dashpot-spring system is firstly built via the analytical dynamics method, where the mechanical force produced by the series inerter-dashpot-spring system is considered as a DOF. Explicit expressions related to the optimal stiffness ratio, optimal mass ratio, and optimal damping ratio for the IDVA as well as the optimal absorber stiffness ratio are then derived using a pole-placement method where the equalized-modal-damping-ratio principle and the triple-root-bifurcation condition are used. These optimal analytical formulas

defining the IDVA type damper are proven to merely depend on the spinning speed of the rotor, given the IDVA location and the absorber mass. The dynamic amplifications for blade displacement, the IDVA-type damper stroke, and the system root locus diagrams are analyzed numerically in comparison with the optimal TMD and optimal RIDTMD. Parametric study for the absorber mass, the rotor speed, the IDVA location is performed. Furthermore, the modal damping ratio for the optimal tuning blade-IDVA system is investigated in comparison with the optimal TMD and optimal RIDTMD. The NREL 5 MW reference wind turbines are used as the numerical example for verifying the effectiveness of the proposed optimal IDVA calibration formulas. Comparison results show that optimal IDVA leads to superior performance than optimal TMD in mitigating the blade edgewise vibration and behaves nearly as same as optimal RIDTMD along with slight deviations in optimal damper parameters. The device is electromagnetically realizable, thus superior than the RIDTMD, due to the eliminated maintenance issues such as oil leakage.

2. Modeling for the Blade-IDVA System

2.1. Problem Definition. Figure 1 demonstrates the model for a rotating blade bonding with an IDVA. A local moving coordinate system (x_1, x_2, x_3) is used to describe the edgewise vibration of the undeformed blade, where x_1 axis is aligned with the along wind direction, x_3 axis is aligned with the undeformed blade axis from the hub to blade tip, and x_2 is determined by the right-hand coordinate rule. Furthermore, a fixed global coordinate system (X_1, X_2, X_3) is introduced to describe the IDVA movement, where it can be defined when x_3 axis in the local moving coordinate system points vertically upwards. The model of each blade for wind turbines is considered using the rotating Euler–Bernoulli beam theory, where $\mu(x_3)$ is the mass per unit length and $EI(x_3)$ is the edgewise bending stiffness.

The azimuthal angle $\Psi(t)$ for a considered blade driven by the rational speed Ω of the rotor can be given as follows:

$$\Psi(t) = \Omega t. \tag{1}$$

The wind-induced edgewise vibration for the blade can be modelled as a degree of freedom (DOF) of $q(t)$, signifying the blade tip displacement, since this vibration is dominated by the fundamental mode. Then, the local displacement $u_2(x_3, t)$ of the rotating blade in the edgewise direction can be described as follows:

$$u_2(x_3, t) = -\Phi(x_3) q(t), \tag{2}$$

where $\Phi(x_3)$ denotes the normalized fundamental mode shape in the edgewise direction, where the normalization is conducted by the tip-mode shape of the blade. The negative means the movement direction of $q(t)$ is opposite to the positive direction of x_2 axis.

In fact, the IDVA is installed inside the rotating blade as shown in Figure 1. The mounted location for the IDVA is assumed at the coordinate $x_3 = x_0$. This provides the blade local displacement at this mounted location:

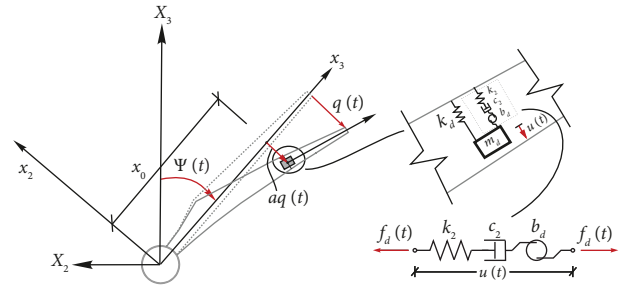

FIGURE 1: The model of the blade-IDVA system.

$$u_2(x_0, t) = -aq(t), \tag{3}$$

where $a = \Phi(x_0)$ is an IDVA position parameter, varying from 0 to 1. It can be determined by the designer, representing the influence of the IDVA location on the blade vibration reduction performance, which has been elaborated in the later section.

The proposed IDVA device is built where the dashpot in the traditional TMD is replaced by a series inerter-dashpot-spring system where the absorber mass and the connected spring stiffness are denoted by m_d and k_d, respectively, as shown in Figure 1. The series system includes a secondary spring with a stiffness of k_2, a linear viscous damper with a damping coefficient of c_2, and an inerter with an inertance of b_d. It should be pointed out that the inerter physical mass can be negligible as opposed to the masses m_d and b_d, benefited from the characteristic of the inerter. For the absorber vibration, $u(t)$ is used to represent the absorber mass displacement with respect to the deformed blade. For the series system, it can produce a mechanical force, denoted as $f_d(t)$, which is considered as a DOF. Hence, the 3-DOF blade-IDVA system of $q(t)$, $u(t)$, and $f_d(t)$ is formed.

The advantage of the proposed IDVA is that this configuration can be realized by not only the mechanical components but also the electrical shunt-based electromagnetic (EM) transducer [33], as given in Figure 2. The EM transducer is one type of electromechanical device [34] exhibiting the electromechanical coupling effects. Supplementing EM transducer with additional shunts (electrical impedances) was proposed with the purpose of realizing a resonant vibration absorber [35–37]. The shunted EM transducers have also been proposed in combination with inertia-based vibration absorber [38, 39] to realize two resonances for improving the vibration control effect. Here, for the shunted EM transducer-based IDVA that is to be installed inside the blade, the shunted EM transducer is introduced to replace the classic dashpot. A series resistive-capacitative-inductive (RCL) network is designed as the supplemental shunt for the EM transducer, where L_s denotes the shunt inductance, R_s is the resistance, and C_s represents the capacitance, as given in Figure 2. The working principle for the shunted EM transducer is that the transducer driven by the blade vibration yields electricity, which can be dissipated by the shunt circuit. The mechanical vibration energy is thereby dissipated, resulting in suppressed blade vibration. In fact, the shunted EM transducer-based IDVA can be

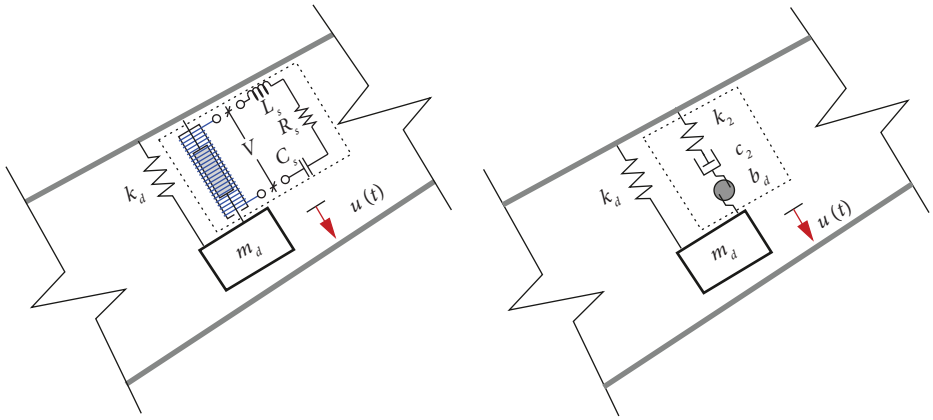

(a) (b)

FIGURE 2: Realization schematic of the IDVA system. (a) The EM transducer with supplemental electrical shunt. (b) The equivalent mechanical model.

equivalently represented by the mechanical structure-based IDVA, and the shunt components are calibrated based on the equivalent mechanical model [33].

2.2. Governing Equation of the Blade-IDVA System. To derive the analytical dynamics for the rotating blade, the Euler–Lagrange equations are introduced to describe the system vibration. The velocity components $v_2(x_3,t)$ and $v_3(x_3,t)$ for a vibrating blade cross-section in the moving local planar coordinate system (x_2,x_3) and the velocity components $V_{2,d}(t)$ and $V_{3,d}(t)$ for the IDVA absorber mass in the fixed global planar coordinate system (X_2,X_3) are first required to build to obtain the system kinetic energy and potential energy, expressed as, respectively.

$$\left.\begin{aligned} v_2(x_3,t) &= -\Omega x_3 - \Phi(x_3)\dot{q}(t) \\ v_3(x_3,t) &= -\Omega\Phi(x_3)q(t) \end{aligned}\right\},$$
$$\left.\begin{aligned} V_{2,d}(t) &= -\left(x_0\Omega + a\dot{q} + \dot{u}\right)\cos\psi + (aq+u)\Omega\sin\psi \\ V_{3,d}(t) &= -\left(x_0\Omega + a\dot{q} + \dot{u}\right)\sin\psi - (aq+u)\Omega\cos\psi \end{aligned}\right\}. \tag{4}$$

These velocity components provide the kinetic energy of the blade-IDVA system.

$$\begin{aligned} T(t) &= \frac{1}{2}\int_0^L \mu(x_3)\left(v_2^2(x_3,t) + v_3^2(x_3,t)\right)\mathrm{d}x_3 + \frac{1}{2}m_d\left(V_{2,d}^2(t) + V_{3,d}^2(t)\right) \\ &= \frac{1}{2}m_0\left(\dot{q}^2 + \Omega^2 q^2\right) + m_1\Omega\dot{q} + \frac{1}{2}\Omega^2 m_2 + \frac{1}{2}m_d\left[\left(x_0\Omega + a\dot{q} + \dot{u}\right)^2 + (aq\Omega + u\Omega)^2\right], \end{aligned} \tag{5}$$

where $m_0 = \int_0^L \mu(x_3)\Phi^2(x_3)\mathrm{d}x_3$ is the blade modal mass, $m_1 = \int_0^L \mu(x_3)x_3\Phi(x_3)\mathrm{d}x_3$ is a mass parameter considering the coupling effect between the rotor rotation and the modal response, and $m_2 = \int_0^L \mu(x_3)x_3^2\mathrm{d}x_3$ represents the mass moment of inertia for the rotating blade relative to the hub.

On the other hand, the potential energy of the blade-IDVA system is expressed as

$$U(t) = m_d g\left(x_0\cos\Psi - aq\sin\Psi - u\sin\Psi\right) + \frac{1}{2}k_0 q^2 + \frac{1}{2}k_d u^2, \tag{6}$$

where g is the gravity acceleration. k_0 represents the blade modal stiffness, given as

$$k_0(\Omega) = \int_0^L \left(EI(x_3)\left(\frac{d^2\Phi(x_3)}{dx_3^2}\right)^2 + N(x_3,\Omega)\left(\frac{d\Phi(x_3)}{dx_3}\right)^2 \right)\mathrm{d}x_3, \tag{7}$$

where $N(x_3, \Omega) = \Omega^2 \int_{x_3}^{L} \mu(\xi)\xi d\xi$ is the centrifugal force per unit length along the blade. This relates to the rotor rotational speed Ω, reflecting the contribution of the centrifugal force to geometric stiffness. Furthermore, the eigenfrequency of the 1st blade edgewise mode is written as follows:

$$\omega_0(\Omega) = \sqrt{\frac{k_0(\Omega)}{m_0}}. \tag{8}$$

Insertion of equations (5) and (6) into the Lagrange equation [40] provides the first two equations of motion related to $q(t)$ and $u(t)$ for the 3-DOF blade-IDVA system.

$$\left(m_0 + a^2 m_d\right)\ddot{q} + am_d\ddot{u} + c_0\dot{q} + \left[k_0 - \left(m_0 + a^2 m_d\right)\Omega^2\right]q - am_d\Omega^2 u = f(t) + am_d g \sin\Psi, \tag{9}$$

$$am_d\ddot{q}(t) + m_d\ddot{u}(t) - am_d\Omega^2 q(t) + \left(k_d - m_d\Omega^2\right)u(t) + f_d(t) = m_d g \sin\Psi, \tag{10}$$

where $c_0 = 2\zeta_0 m_0 \omega_0$ signifies the structural modal damping coefficient in which ζ_0 denotes the modal damping ratio. $f(t)$ signifies the turbulent wind and the gravity-induced modal load. We note that the real blade modal stiffness is smaller than k_0 due to the negative term $-(m_0 + a^2 m_d)\Omega^2$, representing the stiffness softening phenomenon. The same phenomenon also occurs in the IDVA motion.

To facilitate deriving the closed-form tuning formulas, the force $m_d g \sin\Psi$ related to the gravity and the structural damping c_0 are neglected in the following due to the insignificant influence on the damper performance [31]. Assuming harmonic motions, equations (9) and (10) can be rewritten in the frequency domain as

$$\left[-\omega^2\left(m_0 + a^2 m_d\right) + \left(k_0 - \left(m_0 + a^2 m_d\right)\Omega^2\right)\right]q + \left(-\omega^2 am_d - am_d\Omega^2\right)u = f, \tag{11}$$

$$\left(-\omega^2 am_d - am_d\Omega^2\right)q + \left[-\omega^2 m_d + \left(k_d - m_d\Omega^2\right)\right]u + f_d = 0, \tag{12}$$

where ω is the angular frequency under harmonic motion.

For harmonic motions, the force-displacement relation of the series inerter-dashpot-spring system as illustrated in Figure 1 is written as

$$u = \left(\frac{1}{k_2} + \frac{1}{i\omega c_2} + \frac{1}{-\omega^2 b_d}\right)f_d, \tag{13}$$

which leads to the equation of motion for the third DOF f_d:

$$f_d = \frac{-\omega^2 b_d k_2}{-\omega^2 b_d + i\omega b_d k_2/c_2 + k_2}u. \tag{14}$$

In fact, equation (13) representing the mechanical inerter-dashpot-spring system can be converted from a resonant EM absorber obtained by the series RCL-shunt in Figure 2(a), with the following electrical balance equation.

$$V = \left(i\omega L_s + R_s + \frac{1}{i\omega C_s}\right)I, \tag{15}$$

where V denotes the applied loading from the shunt and I is the coil current.

With the following relations,

$$k_2 = \frac{K_m^2}{L_m + L_s},$$
$$c_2 = \frac{K_m^2}{R_m + R_s}, \tag{16}$$
$$b_d = K_m^2 C_s,$$

the electrical balance equation (15) can be converted to the equivalent absorber force relation (14) for the equivalent absorber model in Figure 2(b) with a spring, dashpot, and inerter in series. K_m represents the electromechanical coupling coefficient. L_m is the inductance and R_m is the resistance, in which their series connection represents the inherent impedance of an EM transducer. When an EM transducer operates, a voltage proportional to the velocity is induced and appears across the terminals of the coil

through moving a magnetic core with a given velocity. With a coil as a force actuator, the mechanical force imposed by the EM transducer is proportional to the coil current. Furthermore, the inherent impedance of an EM transducer is generally represented by an inductance in series with an intrinsic loss resistance. The oscillatory voltage amplitude induced by the blade structure motion across the EM transducer must balance the inherent coil impedance and the applied shunt loading. A desired resonant EM absorber can be obtained by the series RCL-shunt containing the shunt inductance, resistance, and capacitance.

Hence, equations (11), (12), and (14) make up the frequency-domain motion equations of the 3-DOF rotating blade-IDVA-coupled system.

3. Optimal Design for the Rotating Blade-IDVA System

In this section, optimal calibration of the IDVA bonded to the blade structure is conducted using a pole-placement method [32, 39, 41, 42] since it is capable of the pole placement for the complex system, providing a series of analytical formulas. Furthermore, the complex system poles can be considered as the roots of the sixth-order characteristic equation, representing the (complex) frequencies of the free vibration modes. Hence, in order to apply the pole-placement method to the 3-DOF rotating blade-IDVA system, its normalized characteristic equation is first deduced in Subsection 3.1. On this basis, the equalized-modal-damping-ratio principle and the triple-root-bifurcation condition (the three root loci of the three modes intersect at a single point) are introduced to achieve the optimal calibration of the IDVA parameters in the form of a set of closed-form formulas, which are presented in Subsections 3.2 and 3.3, respectively.

It should be noted that the pole-placement method can provide simple analytical solutions for the harmonic excitation case, which is an approximation to the H_∞ performance measure [43, 44]. This is different from the case the maximum dynamic amplification is directly minimized, leading to a different frequency tuning and nonexistence of the equal modal damping property, which has been demonstrated [45].

3.1. Normalized Characteristic Equation. To facilitate the later derivation process, the normalized parameters regarding the blade modal mass m_0 and stiffness k_0 are introduced, including the frequency ratio r, absorber mass ratios μ_d, absorber stiffness ratio κ_d, as well as IDVA mass ratio μ, IDVA stiffness ratio κ, and IDVA damping ratio β, as follows:

$$\begin{aligned} r &= \frac{\omega}{\omega_0}, \\ \mu_d &= \frac{m_d}{m_0}, \\ \kappa_d &= \frac{k_d}{k_0}, \\ \mu &= \frac{b_d}{m_0}, \\ \kappa &= \frac{k_2}{k_0}, \\ \beta &= \frac{c_2}{\sqrt{m_0 k_0}}. \end{aligned} \tag{17}$$

Insertion of these expressions into equations (11), (12), and (14) rewrites the equations of motion as

$$\begin{aligned} &\left[-r^2\left(1+a^2\mu_d\right)+1-\frac{1}{\omega_0^2}\left(1+a^2\mu_d\right)\Omega^2\right]q+\left(-r^2 a\mu_d-\frac{1}{\omega_0^2}a\mu_d\Omega^2\right)u=\frac{f}{k_0}, \\ &\left(-r^2 a\mu_d-\frac{1}{\omega_0^2}a\mu_d\Omega^2\right)q+\left[-r^2\mu_d+\kappa_d-\frac{1}{\omega_0^2}\mu_d\Omega^2\right]u+\frac{f_d}{k_0}=0, \\ &\frac{f_d}{k_0}=\frac{-r^2-\mu\kappa}{-r^2\mu+(ir\mu\kappa/\beta)+\kappa}u. \end{aligned} \tag{18}$$

In fact, the structural response amplitude can be represented by its frequency response function. Based on the abovementioned equations, the structural response amplitude normalized by the static response f/k_0 in frequency domain can be expressed as

$$\begin{aligned}\frac{qk_0}{f} = {} & \frac{r^4\mu\mu_d - r^2\left(\mu_d\kappa + \mu\kappa_d + \mu\kappa - \mu\mu_d\Omega_\omega^2\right) + \kappa\kappa_d - \mu_d\kappa\Omega_\omega^2 - ir\left(\mu\kappa/\beta\right)\left(r^2\mu_d - \kappa_d + \mu_d\Omega_\omega^2\right)}{-r^6\mu\mu_d + r^4\left[\mu\mu_d\left(1-2\Omega_\omega^2\right) + \mu_d\kappa + \left(\mu\kappa_d + \mu\kappa\right)\left(1 + a^2\mu_d\right)\right]} \\ & - r^2\left[\mu_d\kappa\left(1-2\Omega_\omega^2\right) - \mu\mu_d C_2 + \left(\mu\kappa_d + \mu\kappa\right)C_1 + \kappa\kappa_d\left(1 + a^2\mu_d\right)\right] + \kappa\kappa_d C_1 - \mu_d\kappa C_2 \\ & + ir\left(\mu\kappa/\beta\right)\left\{r^4\mu_d - r^2\left[\mu_d\left(1-2\Omega_\omega^2\right) + \kappa_d\left(1 + a^2\mu_d\right)\right] + \kappa_d C_1 - \mu_d C_2\right\},\end{aligned} \tag{19}$$

where the three dimensionless parameters are introduced to facilitate equation (19) as follows:

$$\begin{aligned}\Omega_\omega &= \frac{\Omega}{\omega_0}, \\ C_1 &= 1 - \Omega_\omega^2\left(1 + a^2\mu_d\right), \\ C_2 &= \Omega_\omega^2\left(1 - \Omega_\omega^2\right).\end{aligned} \tag{20}$$

Setting the denominator of equation (19) equal to zero then provides the characteristic equation, given as follows:

$$\begin{aligned} & -r^6\mu\mu_d + r^4\left[\mu\mu_d\left(1-2\Omega_\omega^2\right) + \mu_d\kappa + \left(\mu\kappa_d + \mu\kappa\right)\left(1 + a^2\mu_d\right)\right] \\ & - r^2\left[\mu_d\kappa\left(1-2\Omega_\omega^2\right) - \mu\mu_d C_2 + \left(\mu\kappa_d + \mu\kappa\right)C_1 + \kappa\kappa_d\left(1 + a^2\mu_d\right)\right] + \kappa\kappa_d C_1 - \mu_d\kappa C_2 \\ & + ir\frac{\mu\kappa}{\beta}\left\{r^4\mu_d - r^2\left[\mu_d\left(1-2\Omega_\omega^2\right) + \kappa_d\left(1 + a^2\mu_d\right)\right] + \kappa_d C_1 - \mu_d C_2\right\} = 0.\end{aligned} \tag{21}$$

Studies on a classical TMD [30, 41] demonstrate that the optimal design can be achieved by equalizing the two modal damping ratios of the first two free vibration modes. This can also be guaranteed by the condition that the two normalized complex frequencies of the free vibration modes (relative to a reference frequency ω_r) are inverse points with regard to a unit-radius quarter circle. Furthermore, the reference frequency for a classic TMD turns out to be the natural frequency of the rigidly connected blade-TMD combined system [41].

Similarly, a reference frequency ω_r is introduced to further achieve the normalization of the characteristic equation so as to facilitate the root locus calibration. This can be achieved through introducing two new dimensionless ratios: frequency ratio ξ and reference frequency ratio Ω_r, which are defined in the following:

$$\begin{aligned}\xi &= \frac{\omega}{\omega_r} = \frac{r}{\Omega_r}, \\ \Omega_r &= \frac{\omega_r}{\omega_0}.\end{aligned} \tag{22}$$

It should be noted that the parameter ω_r can be considered to be introduced for normalization. This parameter, however, needs to be determined to get the closed-form expressions during the optimal calibration as shown in the following.

Substitution of equation (22) into equation (21) provides the normalized characteristic equation with a sextic polynomial with respect to ξ:

$$
\begin{aligned}
&-\xi^6+\frac{\xi^4}{\Omega_r^2}\left[\left(1-2\Omega_\omega^2\right)+\frac{\kappa}{\mu}+\frac{\kappa+\kappa_d}{\mu_d}\left(1+a^2\mu_d\right)\right]\\
&-\frac{\xi^2}{\Omega_r^4}\left[\frac{\kappa}{\mu}\left(1-2\Omega_\omega^2\right)-C_2+\frac{\kappa+\kappa_d}{\mu_d}C_1+\frac{\kappa\kappa_d}{\mu\mu_d}\left(1+a^2\mu_d\right)\right]+\frac{1}{\Omega_r^6}\left[\frac{\kappa\kappa_d}{\mu\mu_d}C_1-\frac{\kappa}{\mu}C_2\right]\\
&+\frac{i\xi}{\Omega_r}\frac{\kappa}{\beta}\left\{\xi^4-\frac{\xi^2}{\Omega_r^2}\left[\left(1-2\Omega_\omega^2\right)+\frac{\kappa_d}{\mu_d}\left(1+a^2\mu_d\right)\right]+\frac{1}{\Omega_r^4}\left(\frac{\kappa_d}{\mu_d}C_1-C_2\right)\right\}=0.
\end{aligned}
\tag{23}
$$

Two limit states for the IDVA damping, i.e., $\beta \longrightarrow 0$ and $\beta \longrightarrow \infty$, are considered to determine the relationship for different parameters in equation (23). It can be observed that in the complex ξ^2-plane, the roots in the quadratic equation for the third line of equation (23) can be entirely determined as the IDVA damping ratio $\beta \longrightarrow 0$. As the IDVA damping ratio $\beta \longrightarrow \infty$ corresponding to a rigidly combined system, the roots in the cubic equation in the complex ξ^2-plane can be entirely determined.

Once the mass ratio μ_d of the absorber is predetermined, the optimal calibration can be conducted to determine the values of κ_d, κ, β, and μ. First, the equalized-modal-damping-ratio principle in two of the three free vibrational modes is initially introduced, which results in two equations representing the explicit expression of the absorber stiffness κ_d and the relationship among the absorber stiffness κ_d, the IDVA inertance μ, and the IDVA stiffness κ, respectively. Furthermore, the triple-root bifurcation point condition is applied, which provides two extra equations, one representing the relation between the IDVA stiffness κ and the absorber stiffness ratio κ_d and the other one building the relation between the IDVA damping ratio β and the IDVA inertance μ. Based on the abovementioned equations (totally four), the analytical expressions of optimal parameters the IDVA (κ_d, κ, β, and μ) can be finally built.

3.2. Equalized Modal Damping Ratios. In this subsection, the equalized-modal-damping-ratio principle is introduced, i.e., two out of the three roots in the complex ξ^2-plane being inverse points regarding a unit-radius quarter circle (radius being 1). Moreover, this circle intersects with the real axis at $\xi^2 = 1$ and the imaginary axis at $\xi^2 = i$. In terms of the third root, it is located on this unit quarter circle. In fact, IDVA damping ratio β can be assigned with different values, varying from 0 to ∞, which can provide the system root locus diagram. Generally, the root locus diagrams in the ξ^2 domain may be classified into three cases including no bifurcation point, a single bifurcation point, as well as two double-root bifurcation points, as given in Figure 3, which are actually determined by the calibration. The two hollow circles on the horizontal axis represent the two real roots ξ_{0-}^2 and ξ_{0+}^2 of equation (23) as β approaches 0, i.e., $\beta \longrightarrow 0$, and the three square markers are the three real roots $\xi_{\infty-}^2$, 1, and $\xi_{\infty+}^2$ as β approaches ∞, i.e., $\beta \longrightarrow \infty$. The elaboration of Figure 3 will be given in Section 4.3.

The inverse point condition on the real axis can provide the following expressions:

$$
\begin{aligned}
\xi_{\infty-}^2\xi_{\infty+}^2 &= 1,\\
\xi_{0-}^2\xi_{0+}^2 &= 1.
\end{aligned}
\tag{24}
$$

Then, a general quadratic polynomial equation in ξ^2 under the limit $\beta \longrightarrow 0$ can be expressed as

$$
\begin{aligned}
\left(\xi^2-\xi_{0+}^2\right)\left(\xi^2-\frac{1}{\xi_{0+}^2}\right)=0 &\Rightarrow \xi^4-\xi^2\left(\xi_{0+}^2+\frac{1}{\xi_{0+}^2}\right)+1\\
&=0.
\end{aligned}
\tag{25}
$$

It can be observed that the coefficient ratio of the constant term to the 4th-order term is 1. Equalization of this ratio to that in the quadratic equation in ξ^2 in equation (23) under the limit $\beta \longrightarrow 0$ can provide the following relation, given as

$$
\frac{1}{\Omega_r^4}\left(\frac{\kappa_d}{\mu_d}C_1-C_2\right)=1.
\tag{26}
$$

Similarly, the limit $\beta \longrightarrow \infty$ in equation (24) provides a third-order polynomial equation in ξ^2, expressed as

$$
\begin{aligned}
\left(\xi^2-1\right)\left(\xi^2-\xi_{\infty+}^2\right)\left(\xi^2-\frac{1}{\xi_{\infty+}^2}\right)=0 &\Rightarrow \xi^6-\xi^4\left(1+\xi_{\infty+}^2+\frac{1}{\xi_{\infty+}^2}\right)+\xi^2\left(1+\xi_{\infty+}^2+\frac{1}{\xi_{\infty+}^2}\right)-1\\
&=0.
\end{aligned}
\tag{27}
$$

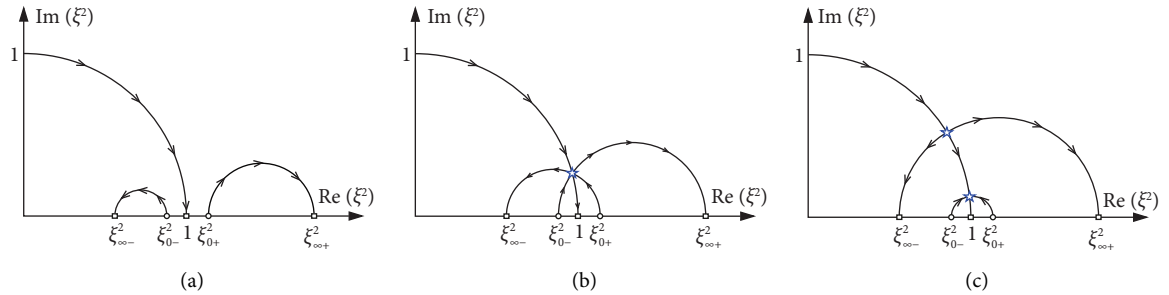

FIGURE 3: Conceptual illustration for three root loci diagrams of the blade-IDVA system. (a) The case without bifurcation point. (b) The case with a single bifurcation point. (c) The case with two double-root bifurcation points. Blue stars: the bifurcation points.

It can be observed from equation (24) that the coefficient ratio of the constant terms to the 6th-order term is −1, and the same ratio is applied to the coefficient ratio of the 2nd-order term to the 4th-order terms. Given the limit $\beta \longrightarrow \infty$, the former condition rewrites equation (23), providing the following expression.

$$\frac{1}{\Omega_r^6}\left(\frac{\kappa\kappa_d}{\mu\mu_d}C_1 - \frac{\kappa}{\mu}C_2\right) = 1, \tag{28}$$

while the latter leads to

$$\frac{1}{\Omega_r^2}\left[\left(1-2\Omega_\omega^2\right)+\frac{\kappa}{\mu}+\frac{\kappa+\kappa_d}{\mu_d}\left(1+a^2\mu_d\right)\right] = \frac{1}{\Omega_r^4}\left[\frac{\kappa}{\mu}\left(1-2\Omega_\omega^2\right)-C_2+\frac{\kappa+\kappa_d}{\mu_d}C_1+\frac{\kappa\kappa_d}{\mu\mu_d}\left(1+a^2\mu_d\right)\right]. \tag{29}$$

Insertion of equations (26) and (28) into equation (29) provides the following expression with respect to the reference frequency ratio Ω_r:

$$\Omega_r^2 = \frac{C_1}{1+a^2\mu_d}, \tag{30}$$

where C_1 has been given in equation (20). It can be observed that $\Omega_r^2 < 1$ for both nonrotating blade and rotating blade under the equalized-modal-damping principle, being different from classical TMD, where the corresponding reference frequency is identical to the eigenfrequency (reference frequency ratio Ω_r being equal to 1) of the combined system.

Based on equations (26) and (28), two equations are obtained as follows:

$$\begin{aligned}\kappa_d &= \mu_d\frac{\Omega_r^4+C_2}{C_1},\\ \mu &= \frac{\kappa}{\Omega_r^2}.\end{aligned} \tag{31}$$

The former equation presents the explicit expression of κ_d, while the latter presents the relation between μ and κ.

3.3. Triple-Root-Bifurcation Condition. In this subsection, the condition that the three root loci intersect at a triple-root-bifurcation point is first applied. To derive the analytical optimal design formulas conveniently, equation (23) can be further simplified by means of utilizing the aforementioned equal modal damping criterion, resulting in

$$-\xi^6+\frac{\xi^4-\xi^2}{\Omega_r^2}\left[\left(1-2\Omega_\omega^2\right)+\frac{\kappa}{\mu}+\frac{\kappa+\kappa_d}{\mu_d}\left(1+a^2\mu_d\right)\right]+1+\frac{i\xi}{\Omega_r}\frac{\kappa}{\beta}\left\{\xi^4-\frac{\xi^2}{\Omega_r^2}\left[\left(1-2\Omega_\omega^2\right)+\frac{\kappa_d}{\mu_d}\left(1+a^2\mu_d\right)\right]+1\right\} = 0. \tag{32}$$

As the limit $\beta \longrightarrow 0$, equation (32) can be further simplified as follows:

$$\xi^4 - \frac{\xi^2}{\Omega_r^2}\left[\left(1 - 2\Omega_\omega^2\right) + \frac{\kappa_d}{\mu_d}\left(1 + a^2\mu_d\right)\right] + 1 = 0. \tag{33}$$

The roots of the quadratic equation in ξ^2 can be obtained as follows:

$$\xi_{0\pm}^2 = C_0 \pm \sqrt{C_0^2 - 1}, \tag{34}$$

with C_0 signifying the algebraic mean value of the two roots when the limit $\beta \longrightarrow 0$ is introduced, expressed as

$$\begin{aligned} C_0 &= \frac{1}{2}\left(\xi_{0+}^2 + \xi_{0-}^2\right) \\ &= \frac{1}{2\Omega_r^2}\left[\left(1 - 2\Omega_\omega^2\right) + \frac{\Omega_r^4 + C_2}{C_1}\left(1 + a^2\mu_d\right)\right]. \end{aligned} \tag{35}$$

Applying equations (26), (28), (30), and (35) to equation (32) provides the following compact form of the full characteristic equation.

$$-\xi^6 + \left(\xi^4 - \xi^2\right)\left(2C_0 + \frac{\kappa C_1}{\kappa_d C_1 - \mu_d C_2} + 1\right) + 1 + \frac{i\xi}{\Omega_r}\frac{\kappa}{\beta}\left(\xi^4 - \xi^2 2C_0 + 1\right) = 0. \tag{36}$$

The triple bifurcation point criterion further rewrites the general polynomial as follows:

$$\left(\xi - \xi_*\right)^3\left(\xi - \overline{\xi}_*\right)^3 = 0, \tag{37}$$

where ξ_* denotes the common root corresponding to the bifurcation point and $\overline{\xi}_*$ is its negative complex conjugate. By means of rewriting equation (37) in a form similar to equation (36) and comparing the coefficients in the two equations, the IDVA stiffness ratio κ_* and damping ratio β_* corresponding to the bifurcation point are obtained

$$\begin{aligned} \kappa_* &= 16\left(C_0 - 1\right)\frac{\kappa_d C_1 - \mu_d C_2}{C_1}, \\ \beta_* &= \frac{\mu\Omega_r}{\sqrt{54\left(C_0 - 1\right)}}. \end{aligned} \tag{38}$$

The triple-root bifurcation point means that the maximum modal damping can be obtained at this triple-root bifurcation point under the equal modal damping criteria, considered as a damping upper limit applied to the system [41]. However, the triple-root bifurcation point presents, indicating angular eigenfrequencies for the three modes are identical. This will cause the constructive interference effect between three modes, which makes calibration at this point not optimal [42]. Instead, a bit lower modal damping ratio will lead to superior vibration reduction for the damper [39]. Therefore, the parameters κ_* and β_* determined using the triple-root bifurcation point criterion need to be tuned with the following two scaling parameters α and η:

$$\begin{aligned} \kappa &= \alpha\kappa_*, \\ \beta &= \frac{1}{\eta}\beta_*, \end{aligned} \tag{39}$$

and these two scaling parameters are determined using numerical optimization methods.

These explicit expressions related to κ_d, κ, μ and β constitute the closed-form optimal calibration for the IDVA bonded to the blade structure. Furthermore, Table 1 presents the full calibration procedure for the rotating blade-IDVA system.

4. Numerical Examples

The rotating blades from the NREL 5-MW reference wind turbine [46] are applied to numerical simulation where each blade is 61.5m in length and its overall mass is 17740kg. The rotor rated rotational speed is $\Omega_0 = 1.27\text{rad}/s$ corresponding to rated wind speed of 11.4m/s and the cut-out wind speed is 25m/s. In practice, the rotor rotational speed remains at rated speed $\Omega_0 = 1.27\text{rad}/s$ for wind speed above rated wind speed of 11.4m/s as a result of the pitch controller. Furthermore, the related data for this wind turbine blade can be found in reference [46].

4.1. Determination of the Scaling Parameters α and β. Figure 4 shows the numerical optimization result for the scaling parameters α and β, where $x_0 = 45\text{m}$ and $\Omega = \Omega_0$ are chosen. The absorber mass ratio μ_d with three different values of 0.01, 0.03, and 0.05 are used, and α is set to vary from 0 to 2. Given α, the optimal η can be obtained through minimizing the maximal blade displacement amplitude $\max\left(|q|k_0/f\right)$. The minimized $\max\left(|q|k_0/f\right)$ with respect to α, under the condition of optimal η, is shown in Figure 4(a). In terms of all μ_d selected, the structural amplitude changes steeply with the slight variation of α when $\alpha < 0.3$. For $\alpha > 0.3$, the structural amplitude increases very slightly with the increase of α. Therefore, an appropriate scaling parameter can be determined based on the trade-off between a relatively small amplitude and a sufficient margin away from the rapid increase. Here, $\alpha = 0.5$ is recommended. The mapping relation of the optimal η as a function of α is shown in Figure 4(b) under different μ_d. As seen, η_{opt} is linearly

Table 1: The full calibration procedure for the blade-IDVA system.

(1)	Choose IDVA location and absorber mass ratio	x_0, μ_d
(2)	Constants C_1 and C_2	$C_1 = 1 - \Omega_\omega^2(1 + a^2\mu_d), C_2 = \Omega_\omega^2(1 - \Omega_\omega^2)$
(3)	Reference frequency ratio Ω_r	$\Omega_r^2 = C_1/(1 + a^2\mu_d)$
(4)	Constant C_0	$C_0 = 1/(2\Omega_r^2)[(1 - 2\Omega_\omega^2) + (\Omega_r^4 + C_2)/C_1(1 + a^2\mu_d)]$
(5)	Absorber stiffness ratio κ_d	$\kappa_d = \mu_d(\Omega_r^4 + C_2)/C_1$
(6)	Choose scaling parameters α and η	Determined by a numerical optimization
(7)	IDVA stiffness ratio κ	$\kappa = \alpha 16(C_0 - 1)(\kappa_d C_1 - \mu_d C_2)/C_1$
(8)	IDVA mass ratio μ	$\mu = \kappa/\Omega_r^2$
(9)	IDVA damping ratio β	$\beta = \mu\Omega_r/(\eta\sqrt{54(C_0 - 1)})$

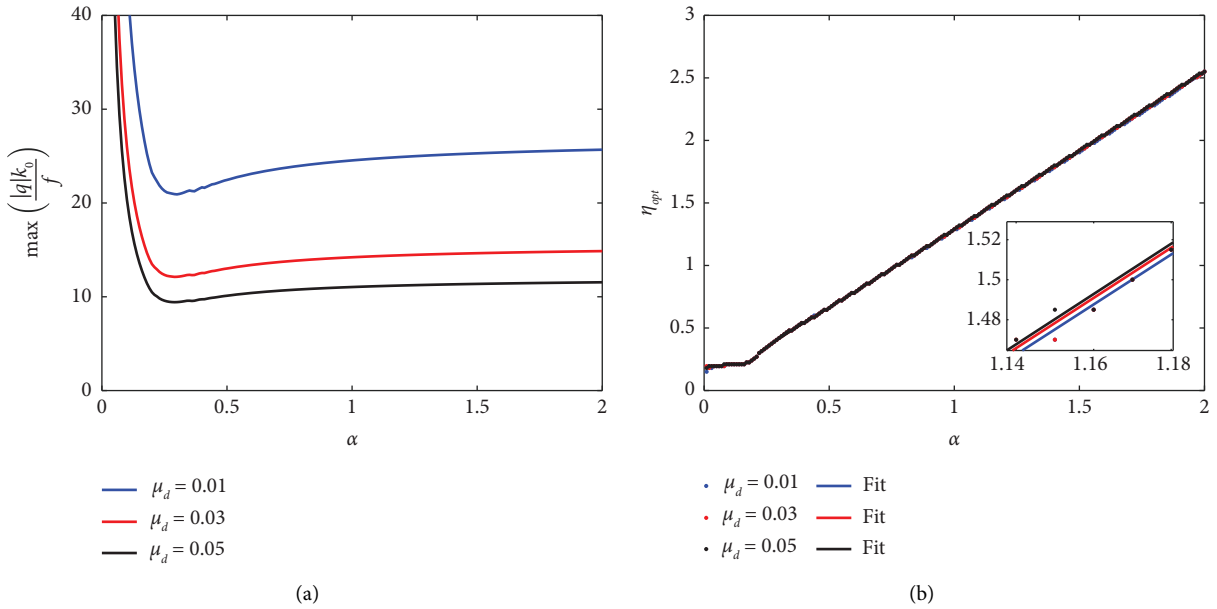

Figure 4: Determination of the scaling parameters α and η, $x_0 = 45$m, and $\Omega = \Omega_0$. The absorber mass ratio μ_d with three different values of 0.01, 0.03, and 0.05 is used. (a) Maximum structural displacement amplitude as a function of α, where the optimal η is applied to minimize $\max(|q|k_0/f)$ given α. (b) Mapping relation of the optimal η with respect to α.

correlated with α, which is almost unrelated to μ_d. Therefore, it can be assumed that this slope is independent on μ_d given small α and a fixed linear relation $\eta_{\text{opt}} = 5/4\alpha + 1/28$ is chosen. Furthermore, the recommended $\alpha = 0.5$ and the linear relation $\eta_{\text{opt}} = 5/4\alpha + 1/28$ are proved to be applied for other realistic values of x_0 and Ω.

4.2. Dynamic Amplification. Figure 5 illustrates the dynamic amplification curves of the blade structural displacement, where $x_0 = 45$m and $\mu_d = 0.03$ are chosen. In order to investigate the influence of α on the IDVA performance, three different values of the scaling parameter α under different rotating speeds Ω are considered following the optimal calibration procedure in Table 1, i.e., $\alpha = 0.2,0.5,1.0$ under each rotating speed Ω. Three cases of rotational speeds Ω are considered, i.e., $\Omega = 0$ corresponding to nonrotating blade, $\Omega = \Omega_0$ corresponding to rated rotating blade, and $\Omega = 3\Omega_0$ considered as an extreme case of rotating blade. As indicated in Subsection 4.1, the optimal α is set to be 0.5 due to the vibration amplitude mitigation performance and its robustness. Furthermore, the linear relation $\eta_{\text{opt}} = 5/4\alpha + 1/28$ holds for varying α.

As seen, the IDVA can effectively reduce the structural response for all considered α. A most flat plateau can be achieved at $\alpha = 0.5$. This indicates optimality, which is in accordance with the classic TMD theory [41]. For $\alpha > 0.5$ ($\alpha = 1$ here), a worsen performance of the IDVA with a higher displacement amplitude is observed in comparison with the case of $\alpha = 0.5$. In fact, a better performance with a lower displacement amplitude can be achieved at $\alpha = 0.3$. However, the maximum dynamic amplification value increases significantly when α changes from 0.3 to 0.2, as also shown in Figure 4(a). In terms of the flat plateau and the robustness against detuning, $\alpha = 0.5$ is considered to be optimal. Comparison among Figures 5(a)–5(c) show that the dynamic amplification curves become broader and move to left as Ω increases, which is also found in the blade-TMD system [30], where $\Omega = 0$ causes fully level plateau and the curves become more skewed as Ω increases.

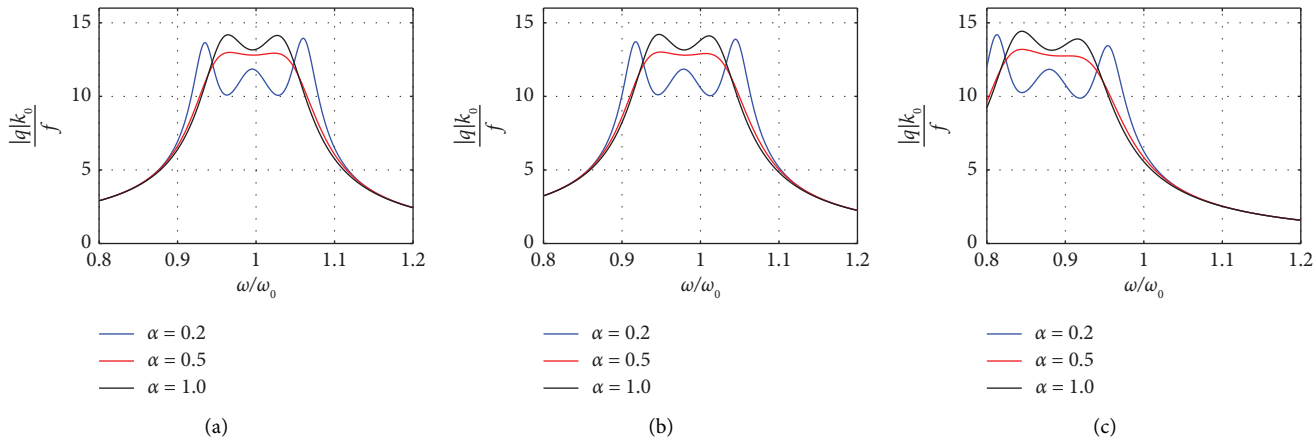

FIGURE 5: Dynamic amplification curves for the structural displacement under different α, where $x_0 = 45$m and $\mu_d = 0.03$. The fitted optimal η is used. (a) $\Omega = 0$. (b) $\Omega = \Omega_0$. (c) $\Omega = 3\Omega_0$.

Figure 6 illustrates the results of the dynamic amplification factor for the relative motion of the absorber. As seen, $\alpha = 0.5$ leads to a fairly flat plateau within which the curves for all considered α are quite similar. However, it is seen that a smaller value of α causes higher peaks of the dynamic amplification, which implies a large absorber stroke. Analogy to the results in Figure 5, the curves become broader and move to left as Ω increases.

Considering the mitigation effect on edgewise vibration for the rotating blade and the relative absorber stroke, the overall performance of the optimally designed IDVA is investigated in comparison with the optimally designed TMD and the rotational inertia double TMD (RIDTMD) [32]. For RIDTMD, the absorber mass is bonded to a parallel inerter-dashpot-spring system in which the inerter in parallel with a dashpot is in series with a spring. The same location and the absorber mass ratio are used. Figure 7 compares the dynamic amplification curves of the blade displacement under the optimal IDVA, the optimal TMD, and the optimal RIDTMD. Following Table 1, the optimal $\alpha = 0.5$ and linear relation $\eta_{\text{opt}} = 5/4\alpha + 1/28$ for IDVA are used. As seen, compared with the optimal TMD, the optimal IDVA can further effectively suppress the edgewise structural displacement, and its plateau presents a more flat and slightly more broad banded. Comparison between IDVA and RIDTMD shows that they have similar vibration damping performance on edgewise vibration of the blade, while the plateau for the IDVA in terms of the dynamic amplification of the structural displacement is more flat than that for the RIDTMD. Comparing Figures 7(a)–7(c) corresponding to different Ω, the vibration damping enhancement for the optimal IDVA, optimal RIDTMD, and optimal TMD are similar. This indicates the efficacy of the optimally designed IDVA using the developed closed-form formulas.

Figure 8 compares the normalized absorber stroke. As shown in Figure 8, the curve for the IDVA is almost the same as the RIDTMD, although slightly flatter. For the peak value, three curves are almost identical. In terms of the plateau, it becomes broader for the IDVA compared with the TMD. This indicates the absorber strokes for the IDVA and RIDTMD are slightly larger than those for the TMD. In application, a large absorber stroke implies a high cost. Therefore, the trade-off between vibration suppression and the cost related to absorber stroke should be considered.

4.3. Root Loci Diagrams and the Resulting Modal Damping Ratios. Figure 9 presents the root loci curves of the 3-DOF rotating blade-IDVA system in ξ^2 domain, which can be obtained by means of varying the IDVA damping ratio β. The case with $x_0 = 45m$, $\mu_d = 0.03$, and $\Omega = \Omega_0$ are used. Furthermore, following Table 1, the optimal $\alpha = 0.5$ and linear relation $\eta_{\text{opt}} = 5/4\alpha + 1/28$ for IDVA are used.

Here, α with three different values of 0.5,1.0,2.0 are considered. The root loci for optimal $\alpha = 0.5$ are shown in Figure 9(a). No bifurcation is observed. For $\beta = 0$, the two roots are placed on the real axis, one at the close left-hand side of 1.0 and one at the close right-hand side of 1.0. When β increases from 0, these two roots move into the imaginary half-plane in the first quadrant. They form two locally enclosed curves ending, respectively, at another two real roots, one at the further left and one at the further right when $\beta \longrightarrow \infty$. On the other hand, the third root (of the total three roots) follows the unit-radius circle ending at 1.0 on the real axis, which exhibits a nonlocal character. Furthermore, an equal modal damping ratio can be confirmed with the fact that the two roots located at the two locally-enclosed curves are inverse points with respect to the unit-radius quarter circle. The red crosses represent the three roots of the 3-DOF system under the optimal β of the IDVA given in equation (39). For the optimally designed IDVA (following the procedure in Table 1), the obtained modal damping ratios of the three modes are, respectively, 0.0415, 0.0415, and 0.0788.

For comparison, the root loci for the optimal TMD and optimally calibrated RIDTMD are plotted with the same x_0, μ_d, and Ω. It can be found that the 2-DOF blade-classic TMD system has a bifurcation point [30]. On the contrary, the 3-DOF blade-RIDTMD system has no

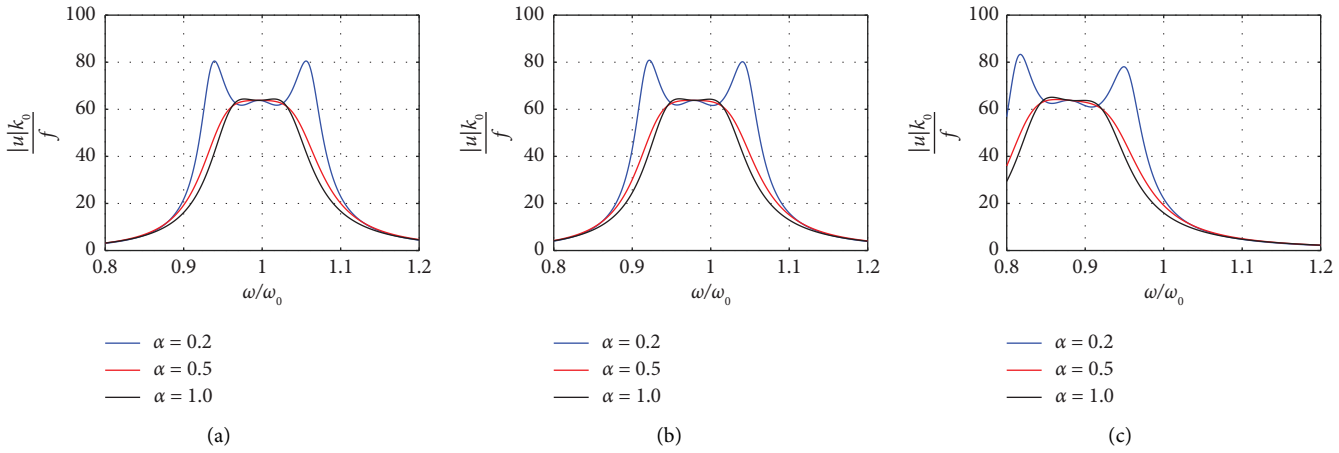

FIGURE 6: Dynamic amplification curves for the relative absorber motion under different α, where $x_0 = 45$m and $\mu_d = 0.03$. The fitted optimal η is used. (a) $\Omega = 0$. (b) $\Omega = \Omega_0$. (c) $\Omega = 3\Omega_0$.

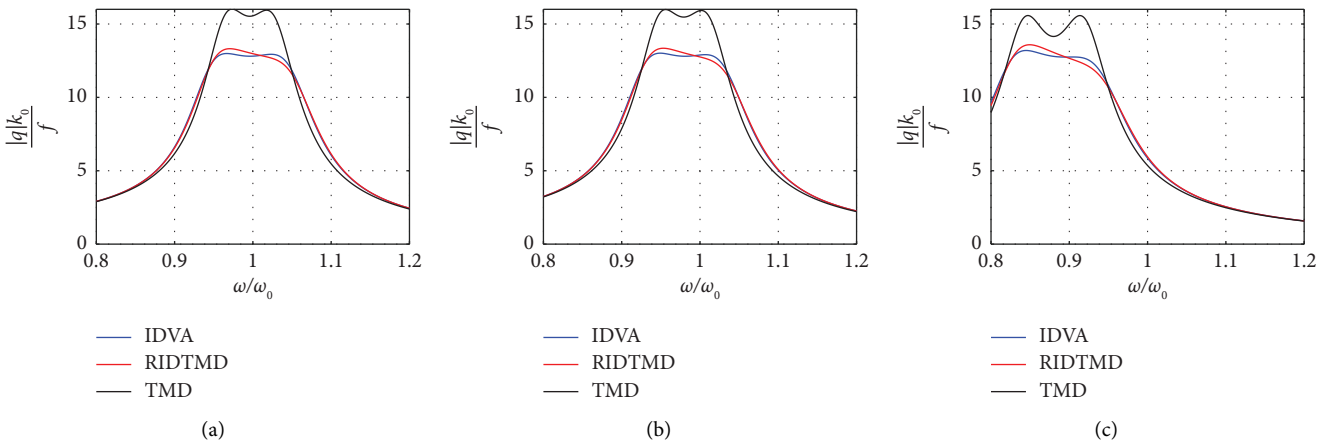

FIGURE 7: Dynamic amplification curves for the structural displacement under the optimal IDVA, the optimal RIDTMD, and the optimal TMD, $\mu_d = 0.03$ and $x_0 = 45$m. (a) $\Omega = 0$ (nonrotating blade). (b) $\Omega = \Omega_0\,(1.27\text{rads}^{-1})$. (c) $\Omega = 3\Omega_0$.

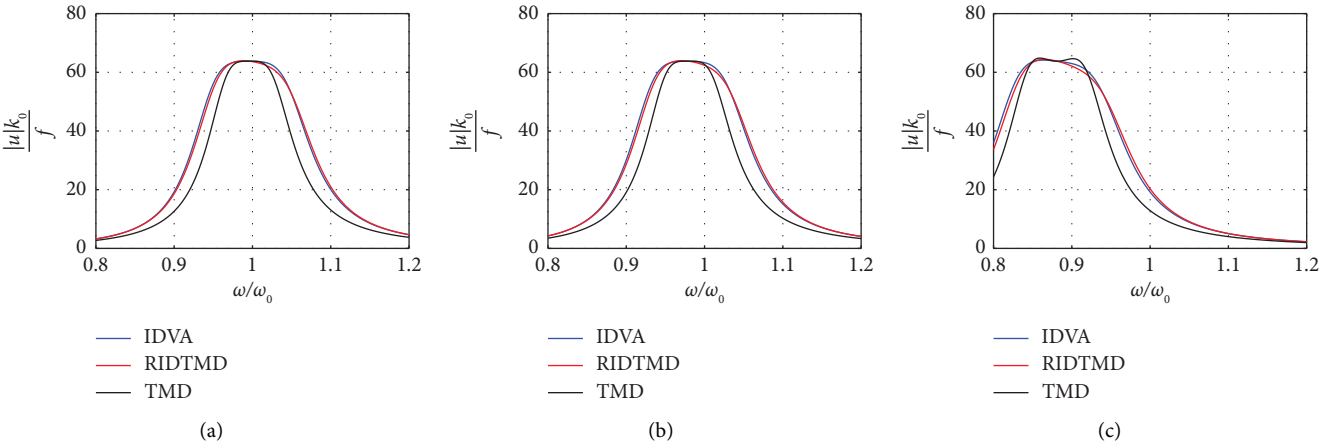

FIGURE 8: Dynamic amplification curves for the absorber stroke under the optimal IDVA, the optimal RIDTMD, and the optimal TMD, $\mu_d = 0.03$ and $x_0 = 45$m. (a) $\Omega = 0$ (nonrotating blade). (b) $\Omega = \Omega_0\,(1.27\text{rads}^{-1})$. (c) $\Omega = 3\Omega_0$.

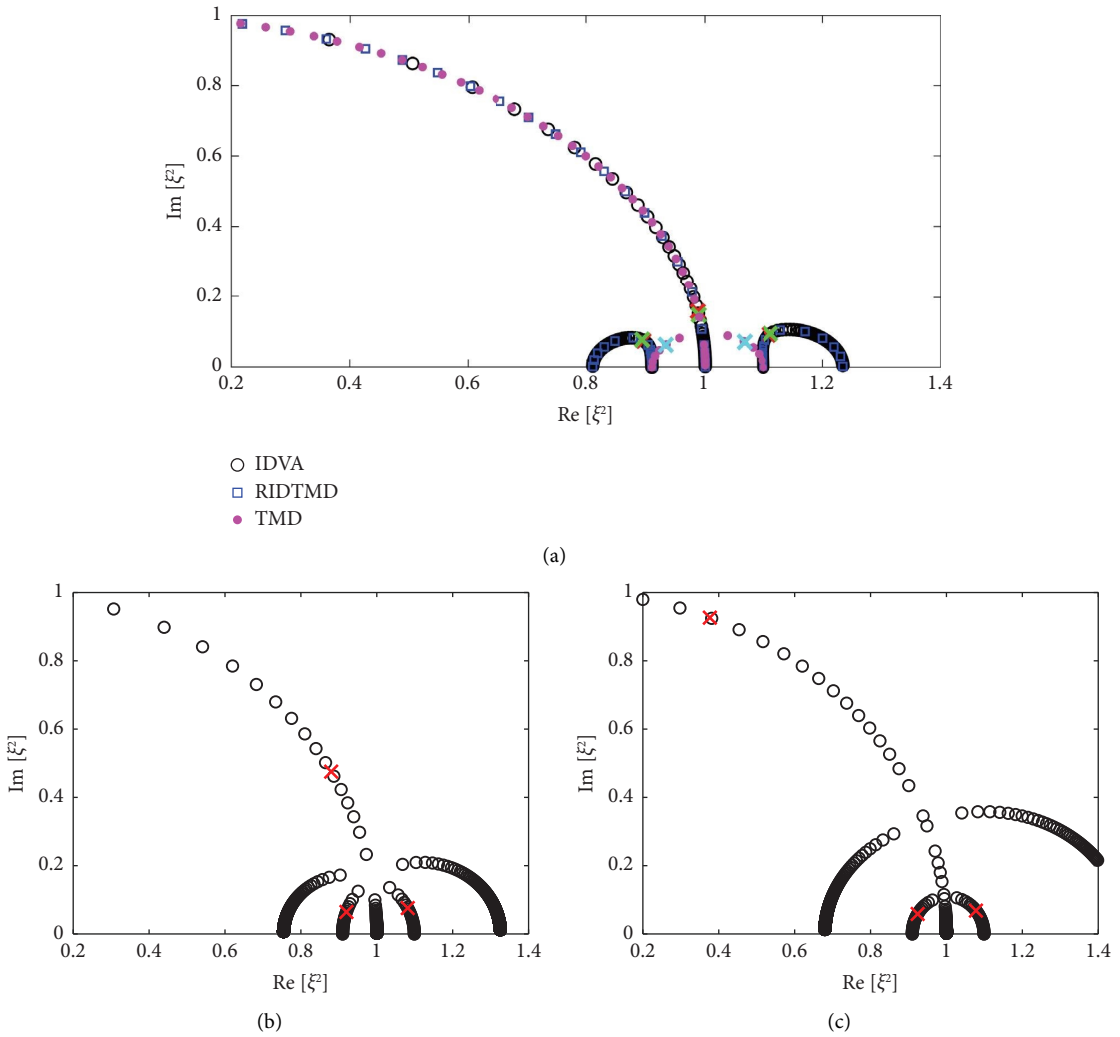

FIGURE 9: Root loci diagrams, $x_0 = 45$m, $\mu_d = 0.03$, and $\Omega = \Omega_0$. Red color crosses indicate the complex roots of the blade-IDVA system for β defined as $\beta = 1/\eta\beta_*$ with $\eta = 5/4\alpha + 1/28$. (a) $\alpha = 0.5$ corresponding to the optimal case. (b) $\alpha = 1.0$. (c) $\alpha = 2.0$.

bifurcation point [32], the same as the blade-IDVA system. Interestingly, the two systems of IDVA and RIDTMD share the unit-radius quarter circle and two enclosed curves as the common root locus diagram, while the arrow directions on the unit-radius circle and enclosed curves for these two systems are opposite. Comparison between IDVA and TMD systems shows that they share the unit-radius quarter circle with the same arrow direction and exactly share the two real roots corresponding to $\beta = 0$, i.e., the zero damping. Furthermore, these two real roots also coincide with the two real roots of the 3-DOF blade-RIDTMD system in the limit $\beta \longrightarrow \infty$. Moreover, the green-color crosses represent the three roots of the blade-RIDTMD system with optimal β (RIDTMD damping ratio), while the cyan-color crosses are two roots of the blade-TMD system with optimal β (TMD damping ratio). The corresponding modal damping ratios are 0.0428,0.0428,0.0736 for optimally calibrated RIDTMD and 0.0332,0.0332 for optimal TMD, respectively.

Figure 9(b) shows the results for $\alpha = 1.0$. One can observe a triple-root bifurcation point, which is consistent with the condition during derivation that the intersection point of three root loci (the bifurcation point) exists when $\alpha = 1.0$. The root loci curves start from two real roots on the horizontal axis for $\beta = 0$ where one is located at the close left of 1.0, one at the close right of 1.0, and end at three different real roots on the horizontal axis in the limit $\beta \longrightarrow \infty$, where one is located at the far left, one at the far right, and one at 1.0. Furthermore, the red crosses represent the three roots under the optimal β. The modal damping ratios for this case are 0.0350, 0.0350, and 0.245, respectively.

Figure 9(c) shows the result for $\alpha = 2.0$. In this case, a pair of double-root bifurcation points is observed at the root loci. Similarly, the root loci curves start from two roots on the real axis for $\beta = 0$ and end at three different real roots in the limit $\beta \longrightarrow \infty$. The red crosses represent the three roots under the optimal β, and the resulting modal damping ratios are 0.0316, 0.0316, and 0.558, respectively.

Table 2: Optimal parameters for the 3-DOF blade-mounted IDVA with $\mu_d = 0.03$.

μ_d	Ω	x_0 (m)	a	IDVA			
				κ_d	κ	μ	β
		20	0.0884	0.0300	2.81×10^{-5}	2.81×10^{-5}	5.35×10^{-4}
	0	30	0.2221	0.0299	1.77×10^{-4}	1.77×10^{-4}	1.34×10^{-3}
		45	0.5269	0.0295	9.83×10^{-4}	9.91×10^{-4}	3.15×10^{-3}
		20	0.0884	0.0300	2.91×10^{-5}	3.01×10^{-5}	5.44×10^{-4}
0.03	Ω_0	30	0.2221	0.0300	1.83×10^{-4}	1.90×10^{-4}	1.36×10^{-3}
		45	0.5269	0.0295	1.02×10^{-3}	1.06×10^{-3}	3.20×10^{-3}
		20	0.0884	0.0300	3.58×10^{-5}	4.57×10^{-5}	6.04×10^{-4}
	$3\Omega_0$	30	0.2221	0.0299	2.26×10^{-4}	2.88×10^{-4}	1.51×10^{-3}
		45	0.5269	0.0296	1.26×10^{-3}	1.62×10^{-3}	3.56×10^{-3}

$\mu_d = 0.03$.

Table 3: Optimal parameters for the 3-DOF blade-mounted IDVA with $\mu_d = 0.05$.

μ_d	Ω	x_0 (m)	a	IDVA			
				κ_d	κ	μ	β
		20	0.0884	0.0500	7.81×10^{-5}	7.81×10^{-5}	1.15×10^{-3}
	0	30	0.2221	0.0498	4.91×10^{-4}	4.92×10^{-4}	2.88×10^{-3}
		45	0.5269	0.0486	2.70×10^{-3}	2.74×10^{-3}	6.72×10^{-3}
		20	0.0884	0.0500	8.07×10^{-5}	8.35×10^{-5}	1.17×10^{-3}
0.05	Ω_0	30	0.2221	0.0498	5.07×10^{-4}	5.26×10^{-4}	2.93×10^{-3}
		45	0.5269	0.0487	2.79×10^{-3}	2.93×10^{-3}	6.84×10^{-3}
		20	0.0884	0.0500	9.95×10^{-5}	1.27×10^{-4}	1.30×10^{-3}
	$3\Omega_0$	30	0.2221	0.0498	6.26×10^{-4}	8.00×10^{-4}	3.26×10^{-3}
		45	0.5269	0.0488	3.46×10^{-3}	4.48×10^{-3}	7.60×10^{-3}

$\mu_d = 0.05$.

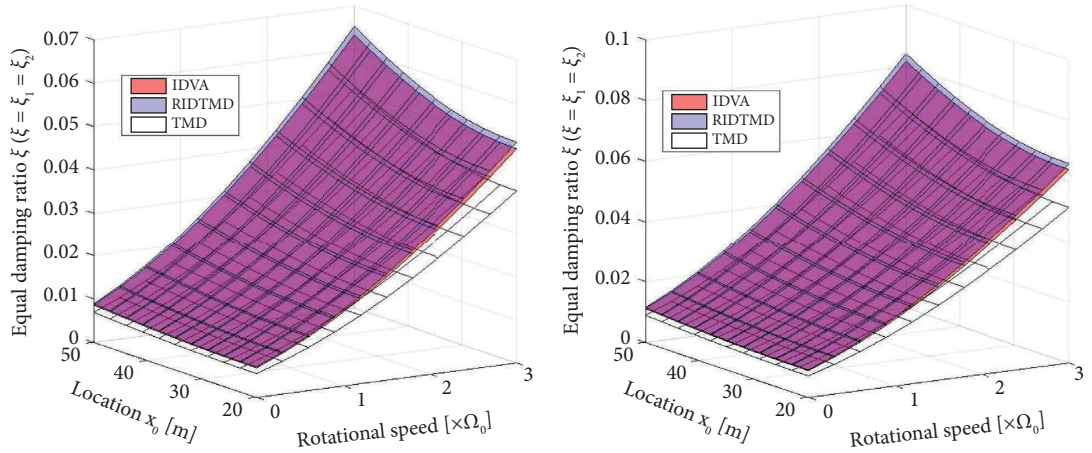

Figure 10: Equal damping ratio as a function of location x_0 and Ω. (a) $\mu_d = 0.03$. (b) $\mu_d = 0.05$.

4.4. Parametric Study. This section will investigate the variation of the parameters κ_d, κ, μ, and β as well as modal damping ratios under different rotational speed Ω, location x_0 equivalently represented by a and absorber mass ratio μ. In the following, rotational speed $\Omega = 0, \Omega_0, 3\Omega_0$, mode shape parameter $a = 0.0884, 0.2221, 0.5269$, and the mass ratio of the absorber $\mu_d = 0.03, 0.05$ are used for three considered systems.

Table 2 gives the optimal IDVA parameters of the 3-DOF rotating blade-IDVA system, under different rotational speed Ω and location x_0. Mass ratio of $\mu_d = 0.03$ is used. As seen, as the location x_0 increases, the optimal absorber stiffness ratio κ_d decreases for all considered rotational speeds, while the other optimal parameters κ, μ, and β increase inversely. For a given location x_0, the optimal absorber stiffness ratio κ_d is almost unchanged as Ω increases

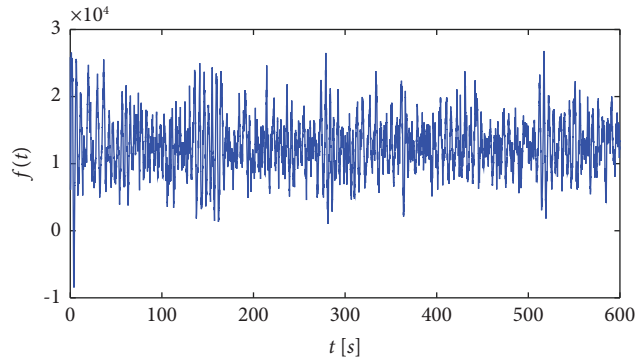

FIGURE 11: Time series of modal load $f(t)$ with wind speed of 15m/s and turbulence intensity of 0.1.

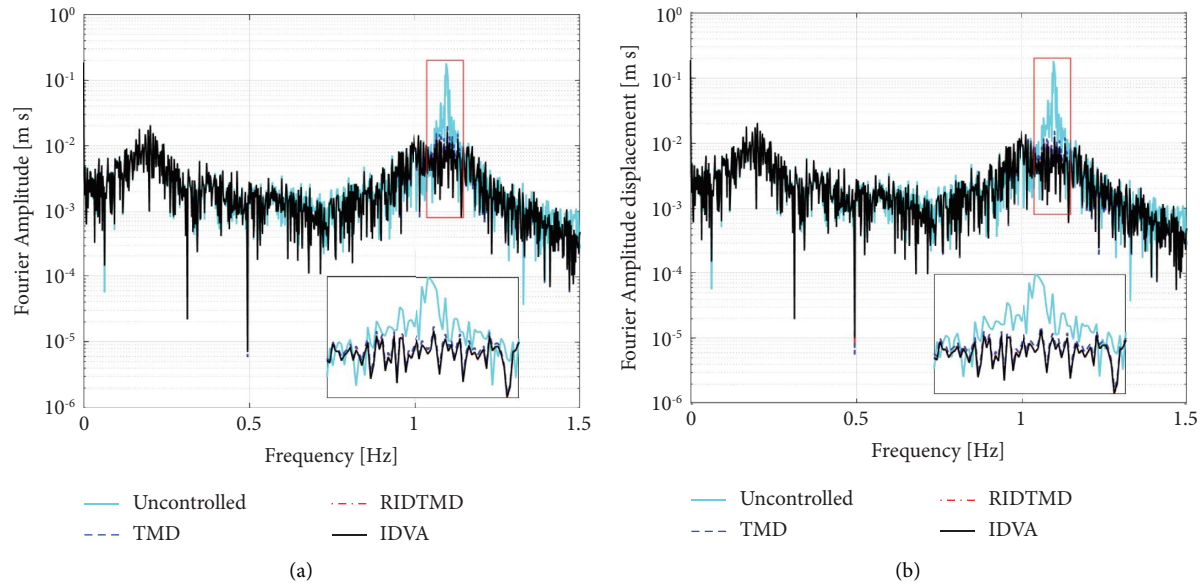

FIGURE 12: Fourier amplitude of $q(t)$ with different mass ratio μ_d. x_0 = 45m. $\Omega = \Omega_0$. (a) $\mu_d = 0.03$. (b) $\mu_d = 0.05$.

and the other IDVA parameters κ, μ, and β slightly increase. This indicates the nonsensitiveness of the optimal IDVA parameters to the variation of rotational speed Ω, which may make a passive IDVA possible, deployed to mitigate blade edgewise vibrations for the considered NREL 5 MW wind turbine. However, for other types of wind turbines with larger changes in rotor rotational speed, a semiactive control strategy may be required due to the variation of the optimal IDVA parameters with the rotational speed. To this end, the coil current can be supplied by tuning the shunt inductance and resistance in the electrical network, corresponding to stiffness and damping in the equivalent mechanical absorber model, respectively.

In order to investigate the effect of the absorber mass on the variation of optimal IDVA parameters, Table 3 shows the results for a large mass ratio $\mu_d = 0.05$. Similar findings for the variation of optimal IDVA parameters κ_d, κ, μ, and β due to location x_0 and rotational speed Ω are found as the case for $\mu_d = 0.03$. Furthermore, comparison for the value of κ_d under different μ_d indicates the variation of the absorber stiffness ratio is to guarantee the IDVA operating close to the blade eigenfrequency. We also find that the variation of the optimal IDVA parameters with the increase of μ_d is similar to that with the increase of x_0. Essentially, increasing μ_d is equivalent to increasing x_0. This can be explained by the fact that $a^2\mu_d$ is present in all the developed design formulas in Table 1 and can be considered as the effective mass ratio.

Figures 10(a) and 10(b) illustrate the equal modal damping ratio ($\xi_1 = \xi_2$) determined using the optimal design formulas for $\mu_d = 0.03$ and 0.05, respectively. Comparison of the resulting modal damping ratios of these three systems (blade-IDVA, blade-TMD, and blade-RIDTMD) shows that the common modal damping ratio of the optimally calibrated blade-IDVA system is always higher than that of the optimally calibrated blade-classic TMD system, while having similar values as the optimally calibrated blade-RIDTMD model given the same rotational speed, absorber location, and absorber mass ratio. This may explain why the IDVA presents the superior performance than the TMD while having similar performance as the RIDTMD in

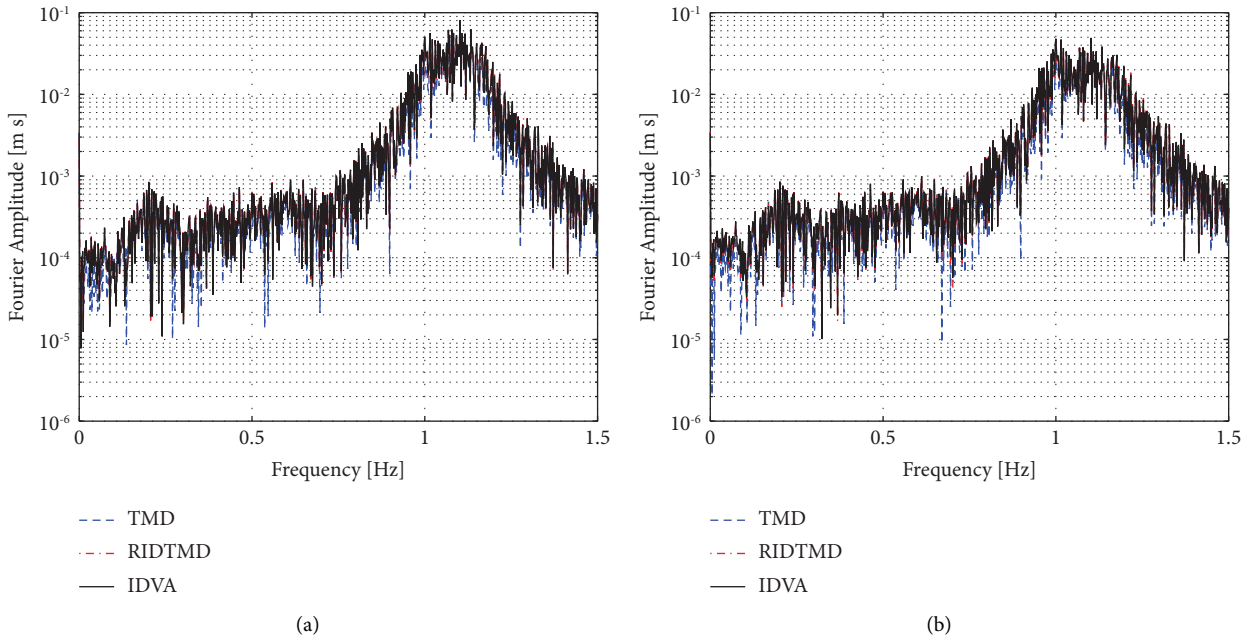

FIGURE 13: Fourier amplitude of absorber stroke with different mass ratio μ_d. x_0 = 45m. $\Omega = \Omega_0$. (a) μ_d = 0.03. (b) μ_d = 0.05.

suppressing blade edgewise vibrations. However, it is worth noting that a greater value of common modal damping ratio does not necessarily signify a better vibration damping efficacy of the IDVA, which can be reflected by the introduction of the scaling parameters.

In order to investigate the damping effect of the IDVA under realistic wind conditions, a mean wind speed of 15m/s and turbulence intensity of 0.1 are considered to generate the rotational sampled turbulence field on the wind turbine rotor [47] using a 13-DOF aero-servo-elastic wind turbine model [16] where the blade edgewise modal load $f(t)$ can be simulated and obtained. Figure 11 shows the time histories of the edgewise modal load $f(t)$. Figure 12 illustrates the performance of the optimally calibrated IDVA for damping the blade edgewise vibration in comparison to the optimally calibrated TMD and RIDTMD in frequency domain (Fourier transformed from the time-domain responses), driven by the modal load $f(t)$ given in Figure 11. Two values of mass ratio μ_d with 0.03 and 0.05 are investigated corresponding to Figures 12(a) and 12(b), respectively. It can be observed that the blade edgewise vibration is fully governed by its fundamental mode because of the low edgewise aerodynamic damping. This can explain why the H_∞ performance measure can be used although the excitation vibration is stochastic. Three absorbers can suppress the blade edgewise displacement $q(t)$ effectively, especially for the spectral peak corresponding to the fundamental edgewise mode of the blade. Furthermore, the IDVA slightly outperforms the TMD and has almost the same damping effect as the RIDTMD. The Fourier amplitude of absorber stroke with different mass ratio of u_d = 0.03 and 0.05 is given in Figure 13. The results indicate that the absorber stroke for the IDVA is slightly increased comparing with the classic TMD, while almost the same as the RIDTMD, which is consistent with the results in Figure 8. In fact, the reduction of the damper stroke can be reduced by means of increasing the damper mass or installing the device closer to blade root at the expense of decreased vibration damping effect.

5. Conclusions

The present paper proposes a new type of inerter-based vibration absorber (IDVA) that can be realized both mechanically and electromagnetically for reducing blade edgewise vibrations. The IDVA consists of an absorber mass bonded to the blade structure and a series inerter-dashpot-spring system. A 3-DOF model has been built for the coupled blade-IDVA system, including the blade tip displacement, the relative displacement of the absorber mass from the deformed structure, and the mechanical force produced by the series inerter-dashpot-spring system. On the basis of on this model, analytical optimal design formulas for the IDVA in terms of the stiffness ratio, mass ratio, and damping ratio for the IDVA, as well as the absorber stiffness ratio, have been derived using the pole-placement method. The equalized modal damping principle, as well as the triple-root bifurcation condition, is used. The developed formulas indicate that all optimal parameters of the IDVA exhibit dependency on the spinning speed of the rotor given the IDVA location and absorber mass.

Comparison for the dynamic amplification curve of the structural displacement shows that the IDVA has superior vibration damping performance on edgewise vibration than the classic TMD while having similar performance with the RIDTMD. We also found that the dynamic amplification curve of the structural displacement for the IDVA is level, which is different from the skewed corresponding curve for the RIDTMD. This, to some extent, indicates the advantage

of IDVA over RIDTMD. Comparison for the absorber stoke shows the absorber strokes for the IDVA and RIDTMD are slightly larger than those for the TMD. Furthermore, the optimally calibrated IDVA results in a root locus diagram with two locally enclosed curves and a unit-radius quarter circle, without the existence of bifurcation points, which is similar as the RIDTMD. However, interestingly, the arrow directions on the unit circle and closed curves for these two systems are exactly opposite. They are all different from the TMD that has a bifurcation point. For the optimally calibrated blade-IDVA system, its common modal damping ratio is consistently higher than that of the blade-classic TMD system (with TMD optimally calibrated), while being very slightly smaller than that of the optimally calibrated blade-RIDTMD system, although it should not be considered as a performance indicator.

Regarding the 5 MW reference offshore wind turbine, it turns out that the calculated optimal IDVA parameters (using the developed formulas) are not very sensitive to rotor rotational speed. Numerical simulations show that the proposed optimal IDVA performs consistently slightly better than the optimal TMD for blade edgewise vibration given the same damper location and absorber mass, while having similar performance with the optimal RIDTMD. This indicates that the inerter-dashpot-spring system can be deployed flexibly for damping rotating blade edgewise vibration. Furthermore, since the proposed IDVA can be achieved by the shunted EM transducer other than being realized mechanically, it can avoid some maintenance issues such as oil leakage.

Nomenclature

ATMD: Active tuned mass damper
CLCD: Circular liquid column damper
EM: Electromagnetic
IDVA: Inerter-based vibration absorber
LCOE: Levelized cost of energy
MR: Magnetorheological
RIDTMD: Rotational inertia double TMD
STFT: Short-time Fourier transform
STMD: Semiactive tuned mass damper
TCD: Tuned liquid damper
TLCD: Tuned liquid column damper
TMDI: Tuned mass-damper-inerter
TMD: Tuned mass damper
C_0, C_1, C_2: Constants
C_s: Capacitance
$EI(x_3)$: Edgewise bending stiffness
I: Coil current
K_m: Electromechanical coupling coefficient
L_m: Inductance for EM transducer
L_s: Shunt inductance
$N(x_3, \Omega)$: Centrifugal force per unit length along the blade
R_m: Resistance for EM transducer
R_s: Resistance
V: Applied loading from the shunt
Ω: Rotor rational speed
Ω_0: Rated rotor rational speed
Ω_r: Reference frequency ratio
$\Phi(x_3)$: Normalized edgewise fundamental mode shape
$\Psi(t)$: Azimuthal angle
α, η: Scaling parameters
β: IDVA damping ratio
κ: IDVA stiffness ratio
κ_d: Absorber stiffness ratio
$\mu(x_3)$: The mass per unit length
μ: IDVA mass ratio
μ_d: Absorber mass ratio
ω_0: Eigenfrequency of the 1st blade edgewise mode
ζ_0: Modal damping ratio
a: IDVA position parameter
b_d: Inertance for inerter
c_0: Structural modal damping coefficient
c_2: Damping coefficient for linear viscous damper
$f(t)$: Turbulent wind and the gravity-induced modal load
$f_d(t)$: Mechanical force from the series system
k_0: Blade modal stiffness
k_2: Spring stiffness in series system
k_d: Connected spring stiffness for absorber mass
m_0: Blade modal mass
m_1: Mass parameter considering the coupling effect between the rotor rotation and the modal response
m_2: Mass moment of inertia for the rotating blade relative to the hub
m_d: Absorber mass
$q(t)$: Blade tip displacement
r: Frequency ratio
$u(t)$: Relative absorber mass displacement
$u_2(x_3, t)$: Local edgewise displacement
x_0: IDVA mounted location.

Data Availability

No data were used to support this study.

Conflicts of Interest

The authors declare that they have no conflicts of interest.

Acknowledgments

The authors gratefully acknowledge the financial support from the National Natural Science Foundations of China (Nos. 02102350077 and 52221002).

References

[1] A. Ahlström, "Influence of wind turbine flexibility on loads and power production," *Wind Energy*, vol. 9, no. 3, pp. 237–249, 2006.

[2] J. Arrigan, V. Pakrashi, B. Basu, and S. Nagarajaiah, "Control of flapwise vibrations in wind turbine blades using semi-active tuned mass dampers," *Structural Control and Health Monitoring*, vol. 18, no. 8, pp. 840–851, 2011.

[3] M. Sayed and M. Kamel, "Stability study and control of helicopter blade flapping vibrations," *Applied Mathematical Modelling*, vol. 35, no. 6, pp. 2820–2837, 2011.
[4] M. Sayed and M. Kamel, "1: 2 and 1: 3 internal resonance active absorber for non-linear vibrating system," *Applied Mathematical Modelling*, vol. 36, no. 1, pp. 310–332, 2012.
[5] D. Ju and Q. Sun, "Wind turbine blade flapwise vibration control through input shaping," *IFAC Proceedings Volumes*, vol. 47, no. 3, pp. 5617–5622, 2014.
[6] K. Thomsen, J. T. Petersen, E. Nim, S. Øye, and B. Petersen, "A method for determination of damping for edgewise blade vibrations," *Wind Energy*, vol. 3, no. 4, pp. 233–246, 2000.
[7] M. H. Hansen, "Aeroelastic instability problems for wind turbines," *Wind Energy*, vol. 10, no. 6, pp. 551–577, 2007.
[8] Z. Zhang, K. A. Hammad, and Y. Song, "Closed-form derivation of aerodynamic damping matrix and pitch vector of an aero-servo-elastic wind turbine system," *Journal of Wind Engineering and Industrial Aerodynamics*, vol. 238, Article ID 105409, 2023.
[9] M. H. Hansen, "Improved modal dynamics of wind turbines to avoid stall-induced vibrations," *Wind Energy*, vol. 6, no. 2, pp. 179–195, 2003.
[10] V. Riziotis, S. Voutsinas, E. Politis, and P. Chaviaropoulos, "Aeroelastic stability of wind turbines: the problem, the methods and the issues," *Wind Energy*, vol. 7, no. 4, pp. 373–392, 2004.
[11] G. Bir and J. Jonkman, "Aeroelastic instabilities of large offshore and onshore wind turbines," *Journal of Physics: Conference Series*, vol. 75, Article ID 12069, 2007.
[12] T. Moeller, "Blade cracks signal new stress problem," *Windpower Monthly*, vol. 25, 1997.
[13] J. Thirstrup Petersen, K. Thomsen, and H. Aagaard Madsen, "Stall strips can control edgewise vibrations," Tech. rep., AED-RB-6, DTU Library, Delhi, India, 1998.
[14] R. Chow and C. van Dam, "Computational investigations of deploying load control microtabs on a wind turbine airfoil," in *Proceedings of the 45th AIAA aerospace sciences meeting and exhibit*, p. 1018, Reno, NV, USA, January 2007.
[15] S. A. Prince, C. Badalamenti, and C. Regas, "The application of passive air jet vortex-generators to stall suppression on wind turbine blades," *Wind Energy*, vol. 20, no. 1, pp. 109–123, 2017.
[16] Z. Zhang, J. Li, S. R. Nielsen, and B. Basu, "Mitigation of edgewise vibrations in wind turbine blades by means of roller dampers," *Journal of Sound and Vibration*, vol. 333, no. 21, pp. 5283–5298, 2014.
[17] Z. Zhang, S. R. Nielsen, B. Basu, and J. Li, "Nonlinear modeling of tuned liquid dampers (tlds) in rotating wind turbine blades for damping edgewise vibrations," *Journal of Fluids and Structures*, vol. 59, pp. 252–269, 2015.
[18] Z. Zhang, A. Staino, B. Basu, and S. R. Nielsen, "Performance evaluation of full-scale tuned liquid dampers (tlds) for vibration control of large wind turbines using real-time hybrid testing," *Engineering Structures*, vol. 126, pp. 417–431, 2016.
[19] B. Basu, Z. Zhang, and S. R. Nielsen, "Damping of edgewise vibration in wind turbine blades by means of circular liquid dampers," *Wind Energy*, vol. 19, no. 2, pp. 213–226, 2016.
[20] Z. Zhang, B. Basu, and S. R. Nielsen, "Tuned liquid column dampers for mitigation of edgewise vibrations in rotating wind turbine blades," *Structural Control and Health Monitoring*, vol. 22, no. 3, pp. 500–517, 2015.
[21] Z. Zhang and C. Høeg, "Dynamics and control of spar-type floating offshore wind turbines with tuned liquid column dampers," *Structural Control and Health Monitoring*, vol. 27, no. 6, Article ID e2532, 2020.
[22] J. Chen, C. Yuan, J. Li, and Q. Xu, "Semi-active fuzzy control of edgewise vibrations in wind turbine blades under extreme wind," *Journal of Wind Engineering and Industrial Aerodynamics*, vol. 147, pp. 251–261, 2015.
[23] H. Biglari and V. Fakhari, "Edgewise vibration reduction of small size wind turbine blades using shunt damping," *Journal of Vibration and Control*, vol. 26, no. 3-4, pp. 186–199, 2020.
[24] H. Biglari and V. Fakhari, "Employing of shunt damping method to reduce edgewise vibration of small size wind turbine blade with considering the effect of vibration coupling," *Amirkabir Journal of Mechanical Engineering*, vol. 53, no. 4, pp. 2073–2088, 2021.
[25] A. Staino, B. Basu, and S. R. Nielsen, "Actuator control of edgewise vibrations in wind turbine blades," *Journal of Sound and Vibration*, vol. 331, no. 6, pp. 1233–1256, 2012.
[26] B. Fitzgerald, B. Basu, and S. R. Nielsen, "Active tuned mass dampers for control of in-plane vibrations of wind turbine blades," *Structural Control and Health Monitoring*, vol. 20, no. 12, pp. 1377–1396, 2013.
[27] S. Krenk, M. N. Svendsen, and J. Høgsberg, "Resonant vibration control of three-bladed wind turbine rotors," *AIAA Journal*, vol. 50, no. 1, pp. 148–161, 2012.
[28] D. Van-Nguyen, B. Basu, and S. Nagarajaiah, "Semi-active control of vibrations of spar type floating offshore wind turbines," *Smart Structures and Systems*, vol. 18, no. 4, pp. 683–705, 2016.
[29] S. Park and M. A. Lackner, "Edgewise vibration suppression of multi-megawatt wind turbine blades using passive tuned mass dampers," *Wind Engineering*, vol. 45, no. 5, pp. 1082–1100, 2021.
[30] Z. Zhang, "Optimal tuning of the tuned mass damper (tmd) for rotating wind turbine blades," *Engineering Structures*, vol. 207, Article ID 110209, 2020.
[31] Z. Zhang and B. Fitzgerald, "Tuned mass-damper-inerter (tmdi) for suppressing edgewise vibrations of wind turbine blades," *Engineering Structures*, vol. 221, Article ID 110928, 2020.
[32] Z. Zhang and T. G. Larsen, "Optimal calibration of the rotational inertia double tuned mass damper (ridtmd) for rotating wind turbine blades," *Journal of Sound and Vibration*, vol. 493, Article ID 115827, 2021.
[33] T. G. Larsen, Z. Zhang, and J. Høgsberg, "Vibration damping of an offshore wind turbine by optimally calibrated pendulum absorber with shunted electromagnetic transducer," *Journal of Sound and Vibration*, vol. 505, Article ID 116144, 2021.
[34] A. Preumont, *Vibration Control of Active Structures: An Introduction*, vol. 246, Springer, Singapore, 2018.
[35] S. Behrens, A. Fleming, and S. R. Moheimani, "Electromagnetic shunt damping," in *Proceedings 2003 IEEE/ASME International Conference on Advanced Intelligent Mechatronics (AIM 2003)*vol. 2, pp. 1145–1150, IEEE, 2003.
[36] S. Behrens, A. J. Fleming, and S. R. Moheimani, "Passive vibration control via electromagnetic shunt damping," *IEEE/ASME transactions on mechatronics*, vol. 10, no. 1, pp. 118–122, 2005.
[37] T. Inoue, Y. Ishida, and M. Sumi, "Vibration suppression using electromagnetic resonant shunt damper," *Journal of Vibration and Acoustics*, vol. 130, 2008.
[38] A. J. Fleming and S. R. Moheimani, "Inertial vibration control using a shunted electromagnetic transducer," *IEEE/ASME Transactions On Mechatronics*, vol. 11, no. 1, pp. 84–92, 2006.
[39] J. Høgsberg, "Vibration control by piezoelectric proof-mass absorber with resistive-inductive shunt," *Mechanics of*

Advanced Materials and Structures, vol. 28, no. 2, pp. 141–153, 2021.

[40] L. A. Pars, *A Treatise on Analytical Dynamics*, Ox Bow Press, Woodbridge, VA, USA, 1979.

[41] S. Krenk, "Frequency analysis of the tuned mass damper," *Journal of Applied Mechanics*, vol. 72, no. 6, pp. 936–942, 2005.

[42] S. Krenk and J. Høgsberg, "Equal modal damping design for a family of resonant vibration control formats," *Journal of Vibration and Control*, vol. 19, no. 9, pp. 1294–1315, 2013.

[43] O. Nishihara and T. Asami, "Closed-form solutions to the exact optimizations of dynamic vibration absorbers (minimizations of the maximum amplitude magnification factors)," *Journal of Vibration and Acoustics*, vol. 124, no. 4, pp. 576–582, 2002.

[44] Y. Hu and M. Z. Chen, "Performance evaluation for inerter-based dynamic vibration absorbers," *International Journal of Mechanical Sciences*, vol. 99, pp. 297–307, 2015.

[45] N. W. Hagood and A. Von Flotow, "Damping of structural vibrations with piezoelectric materials and passive electrical networks," *Journal of Sound and Vibration*, vol. 146, no. 2, pp. 243–268, 1991.

[46] J. Jonkman, S. Butterfield, W. Musial, and G. Scott, "Definition of a 5-mw reference wind turbine for offshore system development," NREL/TP-500-38060, Tech. rep., National Renewable Energy Lab.(NREL), Golden, CO, USA, 2009.

[47] M. N. Svendsen, S. Krenk, and J. Høgsberg, "Resonant vibration control of rotating beams," *Journal of Sound and Vibration*, vol. 330, no. 9, pp. 1877–1890, 2011.